RSC Advances

PAPER

View Article Online
View Journal | View Issue

Cite this: *RSC Adv.*, 2025, **15**, 9627

Construction of a Rh-doped $SrTiO_3$/g-C_3N_4 p–n heterojunction for enhanced photoelectrochemical performance†

Feng Nan, *[a] Songtao Chen,[a] Shun Wang,*[b] Yi Lin,[a] Baolu Fan,[a] Hao Li *[c] and Lei Zhou *[a]

Semiconductor photoelectrochemical (PEC) technology, capable of generating hydrogen energy from water and solar energy, has emerged as a promising solution to address environmental and energy challenges. Rhodium-doped strontium titanate (Rh doped $SrTiO_3$, RST) is regarded as a highly promising photocathode material for PEC systems. Nevertheless, the PEC performance of RST is hindered by inefficient carrier separation and poor charge transfer properties. In this paper, a hybrid RST/g-C_3N_4 heterojunction sample was prepared by a simple method. The pure RST sample possesses the ability to absorb visible light and exhibit p-type semiconductor characteristics with a negative photocurrent value of −6.2 μA cm^{-2}, and can be used as a photocathode material in PEC systems. The enhanced PEC performance with larger photocurrent values can be observed in the heterojunction samples. A photocurrent value of −26.5 μA cm^{-2} was achieved in the optimized heterojunction, which is 4.3 times higher than the RST sample. This enhanced PEC performance can be attributed to the formation of a p–n junction between RST and g-C_3N_4 in composite samples. The p–n junction with built-in electric field and good band alignment will facilitate the more efficient separation and transfer of carriers, leading to enhanced PEC performance.

Received 17th October 2024
Accepted 23rd March 2025

DOI: 10.1039/d4ra07440h

rsc.li/rsc-advances

1. Introduction

In the last few decades, semiconductor photoelectrochemical (PEC) technology has attracted great attention due to its production of hydrogen (H_2) from water and solar energy.[1–4] Recently, the development of photoelectrodes that can absorb visible light, which accounts for approximately 45% of the total solar energy, has been the research focus. Several semiconductor photoelectrodes, including WO_3, Fe_2O_3, and $BiVO_4$, have been developed for PEC water splitting, leveraging their visible-light absorption capabilities.[5–7] These oxide photoelectrodes exhibit an inadequate conduction band level for H_2 evolution with an n-type semiconductor character. Therefore, an external bias is necessary for water splitting in PEC systems utilizing these photoelectrodes. Rhodium-doped strontium titanate (Rh doped $SrTiO_3$, RST) photoelectrode materials exhibit the ability to absorb visible light, with their conduction band levels exceeding the redox potential required for H_2 evolution. Consequently, they are suitable as photocathodes for hydrogen production in PEC systems, attributed to their p-type semiconducting properties.[8–12] The visible light absorption ability of RST can be attributed to electronic transitions from the Rh^{3+} (donor levels) to the conduction band (Ti 3d orbitals) and the electronic transitions from valence band (O 2p) to Rh^{4+} (acceptor levels).[13–16] However, the photoelectric conversion efficiency is still limited due to the high recombination rates and poor transfer properties of carriers in RST. To address the issues, coupling RST with other materials to form a heterostructure has emerged as an efficient strategy.[17–21]

Recently, n-type graphitic carbon nitride (g-C_3N_4), known for its thermal and chemical stability, has emerged as a promising material in the field of photocatalysis. As an excellent visible light photocatalyst, g-C_3N_4 possesses a suitable bandgap of 2.7 eV, with band potentials well-suited for water splitting, making it an ideal candidate for renewable energy generation.[22,23] However, pure g-C_3N_4 faces challenges in separating photogenerated charges and exhibits low electrical conductivity, resulting in suboptimal photocatalytic performance. Constructing a p–n heterojunction can utilize the internal electric field to prevent the rapid recombination of photogenerated carriers, thereby enhancing photocatalytic activity. Various semiconductor/g-C_3N_4 p–n heterojunctions (such as

[a]*Faculty of Mathematics and Physics, Huaiyin Institute of Technology, Huaian, 223003, Jiangsu, China. E-mail: fengnan@hyit.edu.cn; leizhou@hyit.edu.cn*
[b]*School of Electronic and Information Engineering, Changshu Institute of Technology, Suzhou, 215000, Jiangsu, China. E-mail: swang@cslg.edu.cn*
[c]*State Key Laboratory of Radio Frequency Heterogeneous Integration, College of Physics and Optoelectronic Engineering, Key Laboratory of Optoelectronic Devices and Systems of Ministry of Education and Guangdong Province, Shenzhen University, Shenzhen, 518060, Guangdong, China. E-mail: lihao000000@163.com*

† Electronic supplementary information (ESI) available. See DOI: https://doi.org/10.1039/d4ra07440h

NiO/g-C_3N_4, $CoFe_2O_4$/g-C_3N_4, Co_3O_4/g-C_3N_4 and Mn_3O_4/g-C_3N_4) have been developed to reduce carrier recombination rates.[24–27] In the past decade, RST and g-C_3N_4 composites have been extensively utilized in photocatalysis. For instance, Wang *et al.* prepared the RST and phosphorus doped g-C_3N_4 composites by calcination treatment.[28] The results possessed the rational band alignment can greatly promote the charge separation and thus leading to the superior activity for H_2 production in composites. Kumar *et al.* fabricated the 3D superstructure of g-C_3N_4/RGO/RST for H_2 production.[29] The higher catalytic activity can be attributed to the well-matched energy band positions, facilitating efficient charge transfer in composite photocatalysts. However, there was lacking research on the dynamics and PEC performance of p–n junction photoelectrodes by combining p-type RST to n-type g-C_3N_4.

In this work, we design and fabricate RST and g-C_3N_4 composite photoelectrodes using a straightforward scraping coating technique. The scraping coating method presents potential advantages for large-area electrode fabrication, including simplicity, low cost, and broad applicability. The experimental data demonstrates that incorporating g-C_3N_4 materials forms p–n junctions in the RST and g-C_3N_4 composites, significantly improving the PEC properties. The pure RST photoelectrode sample has a photocurrent value of -6.2 μA cm^{-2} with the p-type characters in PEC measurement. The maximal value of -26.5 μA cm^{-2} exhibited in the RSTCN7.5 sample, which was 4.3 times than that of RST sample. The enhanced PEC performance can be attributed to the formed p–n junction between RST and g-C_3N_4, which will improve the dynamics of carrier separation and transport, leading to larger photocurrent values in heterojunction photoelectrodes. Our experimental results provide a facile and effective method for integrating p–n heterojunction materials into PEC applications.

2. Materials and methods

2.1 Chemical and materials

$SrCO_3$ (99.9%), TiO_2 (99.9%), and melamine (99%) were purchased from Sigma Aldrich. Rh_2O_3 (99.9%) was purchased from J&K Scientific. Na_2SO_4 (99%) and ethanol (99.7%) were obtained from Sinopharm chemical reagent Co. Ltd. All chemicals were used for the experiments without further purification. Fluorine-doped SnO_2 (FTO) glass substrates were purchased from South China Xiang Cheng Technology Co. Ltd, and deionized water can be obtained from local sources.

2.2 Preparation of photoelectrodes

In this study, $SrTiO_3$ doped with Rh was prepared by the solid-state reaction.[10] Considering the influence of Rh doping on the onset potential of the RST sample, we chose 2.5% Rh doping.[16] The starting materials, $SrCO_3$ (1.5796 g), TiO_2 (0.7790), and Rh_2O_3 (0.0317 g), were mixed at an agate mortar and the chemical formula was $Sr(Ti_{0.975}Rh_{0.025})O_3$. Then, the mixtures were calcined at 900 °C for 1 h and at 1100 °C for 10 h in air. The obtained powders are labeled as RST. The pure $SrTiO_3$ powder was prepared by the same method without Rh doping. The g-C_3N_4 was synthesized *via* the thermal polymerization method by heating melamine at 550 °C for 4 h in air. The prepared RST and g-C_3N_4 powders were mixed with 50 mL of deionized water and stirred continuously for 10 hours to achieve homogeneous suspensions. The suspensions were dried at 80 °C and then calcined at 450 °C for 2 hours in air. During this process, the weight percentages of g-C_3N_4 in the RSTCN composites were controlled at 2.5%, 5%, 7.5%, and 10%. Accordingly, the resulting samples were named RSTCN2.5, RSTCN5, RSTCN7.5, and RSTCN10.

The FTO substrates were sequentially cleaned by ultrasonic cleaning with acetone, ethanol, and deionized water, respectively, and then the FTO substrates were dried for further use. The photoelectrodes were prepared by the simple knife scraping method. Briefly, 50 mg RSTCN composites powder and 100 μL ethanol solution for grinding to obtain the slurry. Then the slurry materials were scraped on the FTO substrate with the annealing treatment at 450 °C for 2 hours in air. Pure RST photoelectrodes were also synthesized using the same method. The annealing process will have a positive effect on the adhesion between the FTO substrates and photoelectrode materials, also will facilitate the transfer of charge carriers in sample. Pure g-C_3N_4 photoelectrodes were prepared using the scrape method. A mixture of 50 mg of g-C_3N_4 powder and 100 μL of ethanol containing 0.5 wt% Nafion was ground in an agate mortar to form a viscous slurry. This slurry was applied to FTO substrates and calcined at 200 °C for 2 hours in air. The addition of Nafion and low-temperature annealing helps prevent the detachment of g-C_3N_4.

2.3 Characterization methods

The morphology structures were investigated by field emission scanning electron microscope (FESEM, Hitachi S8100) and transmission electron microscope (TEM, Tecnai G2 F20). Fourier transform infrared (FTIR) spectra were measured on a Varian 3600 FTIR spectrometer. The X-ray diffraction (XRD) patterns were measured by Bruker D8 Advance X-ray diffractometer equipped with Cu Kα radiation ($\lambda = 1.540598$ Å) to analyze the crystal structures of different samples. The X-ray photoelectron spectrometer (XPS, PerkinElmer PHI 5000) curves were measured to determine the chemical states and valence band spectra for different samples. And the C 1s peak of 284.80 eV served as a reference for calibration and correction. The optical absorption spectra of different samples were obtained by the UV/Vis/NIR Spectrometer (PerkinElmer Lambda 750). The photoluminescence (PL) spectra were conducted by the steady fluorescence spectrometer (FLS1000, Edinburgh) at the excitation wavelength of 320 nm.

2.4 Photoelectrochemical measurement

The CHI-660E electrochemical workstation was used to evaluate the PEC performance on different samples in a standard three-electrode system. The photoelectrodes served as the working electrode, while the Pt wire and Ag/AgCl electrode functioned as the counter and reference electrodes, respectively. The 0.5 mol L^{-1} aqueous solution of Na_2SO_4 was chosen as the

electrolyte. The light source is a 300 W Xe lamp, and the light intensity was controlled at 100 mW cm^{-2}. Electrochemical impedance spectroscopy (EIS) was measured within the frequency range of 0.01 Hz to 10 kHz, applying a 10 mV AC voltage. The Mott–Schottky plots were carried out at a fixed frequency of 1000 Hz.

3. Results and discussion

3.1 Morphology and structure characterization

Fig. 1a displays the morphology of pure RST with an irregular particle shape. After decorating with g-C_3N_4 materials, there are some subtle but obvious changes in RSTCN7.5 sample. The curved materials were the existence of g-C_3N_4 in RSTCN7.5 sample. As shown in Fig. 1c, the XRD patterns were carried out to observe the crystal structure of different samples. For the RST sample, diffraction peaks corresponding to the crystal planes (100), (110), (111), (200), (210), (211), (220), and (310) were observed, with their positions and relative intensities consistent with the JCPDS No. 35-0634.[16] However, the diffraction peaks of g-C_3N_4 were not observed in the RSTCN7.5 sample, which may be caused by the small amount of g-C_3N_4 in composites. The Fig. 1d shows the FTIR spectra of different samples. For the RST, the peak of Ti–O bond can be observed at 600 cm^{-1}. For the RSTCN7.5 sample, in addition to the peak of Ti–O bond, there are other peaks attributed to g-C_3N_4. The peaks located at 810 cm^{-1} and 1200–1600 cm^{-1} can be assigned to the breathing vibration of triazine units and the C–N/C=N bonds, respectively.[28] The morphology and FTIR spectra for g-C_3N_4 are displayed in Fig. S1.† Based on above analysis, we have successfully prepared the RSTCN heterojunction samples.

3.2 Chemical states analysis

As shown in Fig. 2, the chemical states of the elements for RST and RSTCN7.5 samples were measured by the XPS spectra. For pure RST sample, the peaks located at binding energy of 309.76 eV, 314.54 eV, 132.90 eV, 134.55 eV, 458.79 eV, and 464.61 eV were observed, which can be assigned to the Rh $3d_{5/2}$, Rh $3d_{3/2}$, Sr $3d_{5/2}$, Sr $3d_{3/2}$, Ti $2p_{3/2}$, and Ti $2p_{1/2}$, respectively.[30] After decorating with g-C_3N_4 materials, a shift towards lower binding energy can be observed on the Rh 3d, Sr 3d, and Ti 2p in RSTCN composites. The negative shift towards lower binding energy can be attributed to the electronic interaction between RST and g-C_3N_4, and the RST materials obtains electrons from the g-C_3N_4.[31,32] For RSTCN7.5 heterojunction sample, the deconvoluted high-resolution C 1s spectra have three peaks at binding energy positions of 284.80, 285.70, and 288.12 eV, which can be assigned to C=C, C–C/C–N and N–C=N, respectively.[33,34] In addition, the high-resolution N 1s spectra can be deconvoluted into three peaks at binding energy positions of 398.61 eV (C=N–C), 399.49 eV (N–$(C)_3$), and 401.23 eV (H–N–C), respectively.[24] Based on the XPS analysis, the prepared heterojunction samples are not a simple mixture of two components, and the XPS analysis also confirmed the successfully preparation of RST/g-C_3N_4 heterostructures.

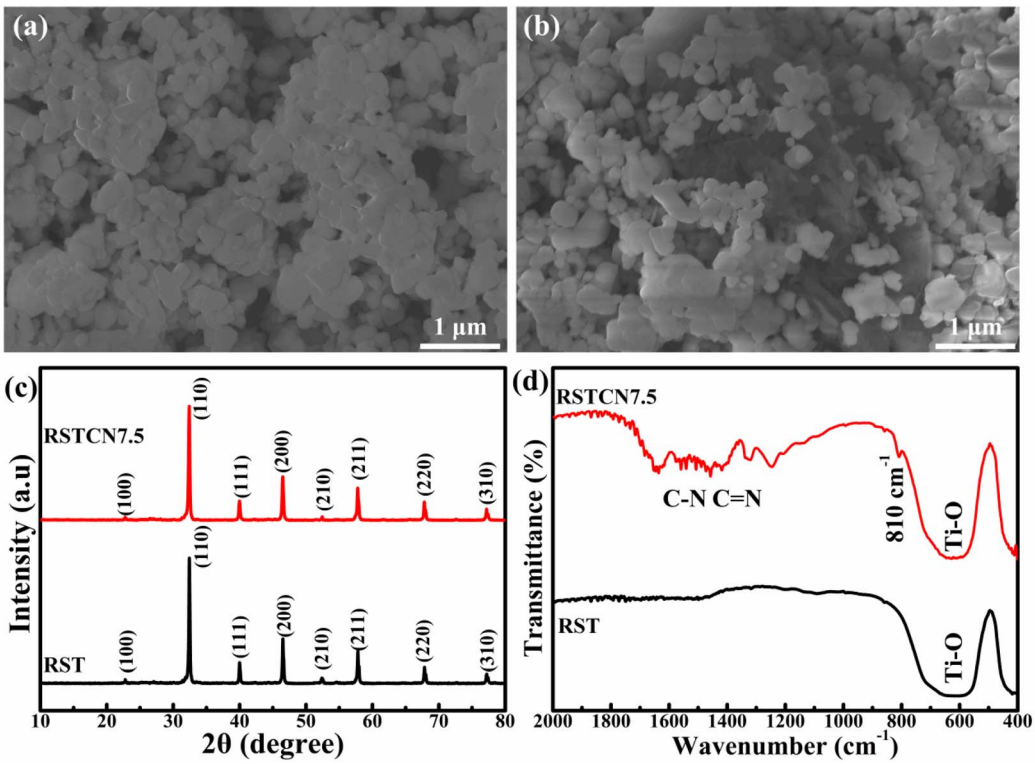

Fig. 1 Basic structure characterisation of different samples. SEM images for (a) pure RST and (b) RSTCN7.5 sample. (c) XRD patterns of RST and RSTCN7.5 samples. (d) FTIR spectra of RST and RSTCN7.5 samples.

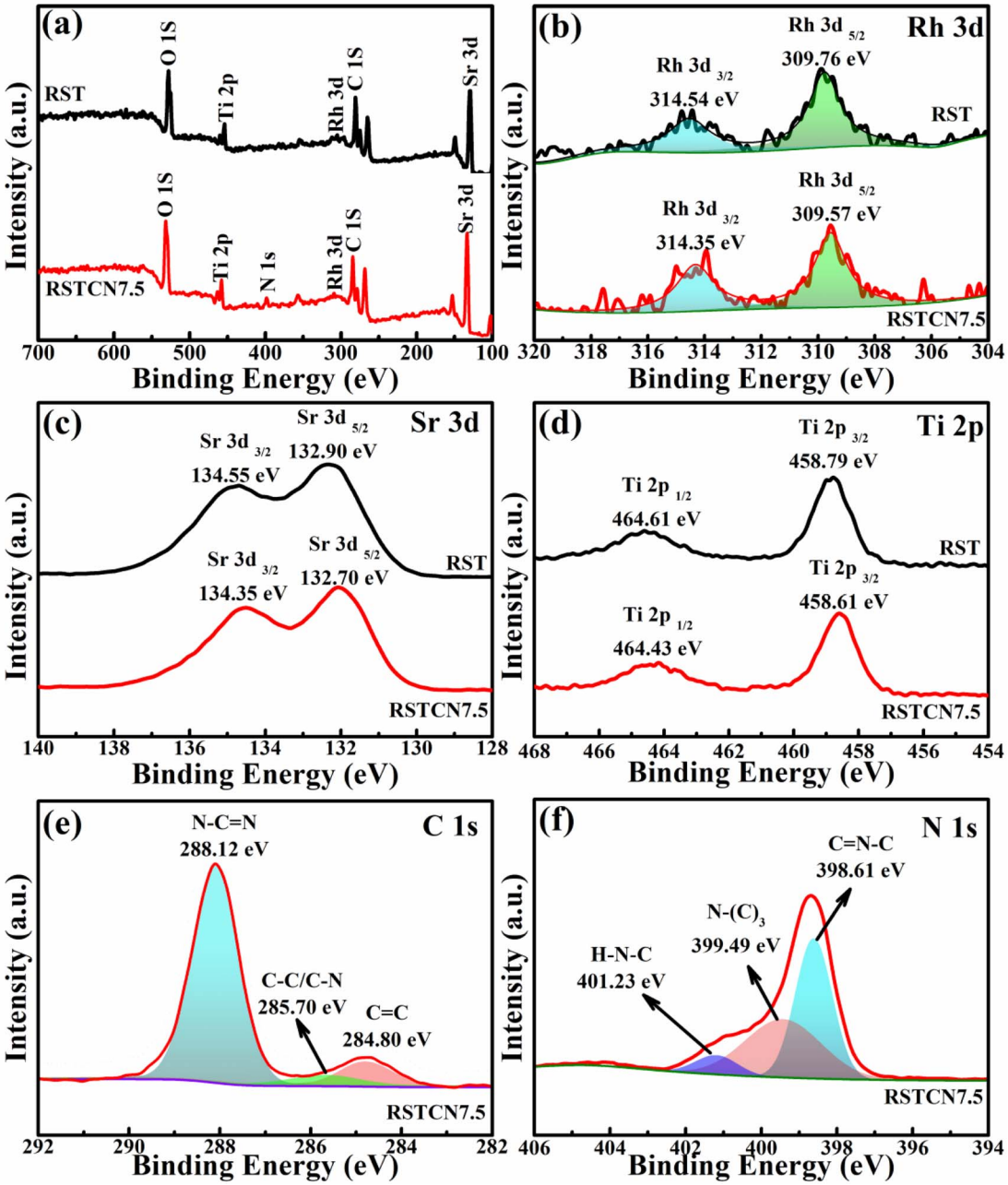

Fig. 2 XPS analysis of different samples. (a) XPS survey spectra, high resolution XPS spectra of (b) Rh 3d, (c) Sr 3d, (d) Ti 2p, (e) C 1s, and (f) N 1s.

3.3 Photoelectrochemical measurements

Fig. 3a–e display the measured current density *versus* time curves of different samples under chopped light irradiation, respectively. All the samples exhibit the clear photoelectric response. A negative photocurrent value of about -6.2 μA cm^{-2} (at 0 V *versus* Ag/AgCl) was investigated in pure RST sample, implying its p-type semiconductor characteristic. In the PEC measurement (Fig. S3†), pure g-C_3N_4 exhibited a lower negative photocurrent value. Consequently, the semiconductor characteristics of various materials will be further verified using Mott–Schottky curves and valence band spectra. After decorating with g-C_3N_4, all the composite heterojunction photoelectrodes show the enhanced PEC properties with the larger photocurrent values. By increasing the contents of g-C_3N_4 materials, the RSTCN heterojunction samples show an improved photocurrent density and a maximal value of -26.5 μA cm^{-2} (at 0 V *versus* Ag/AgCl) in the optimized RSTCN7.5 heterojunction sample, which is 4.3 times than that in pure RST. However, the reduction of photocurrent density value will be investigated with the further increase of g-C_3N_4 materials content. It is important to note that the simplicity and low cost of the scraping method used for powder photoelectrodes in this study resulted in photocurrent values as low as microamperes. The PEC properties were inferior to those of other photocathode samples, such as Si and Cu_2O photocathodes, as well as the high-quality RST thin film photoelectrode prepared by the molecular beam

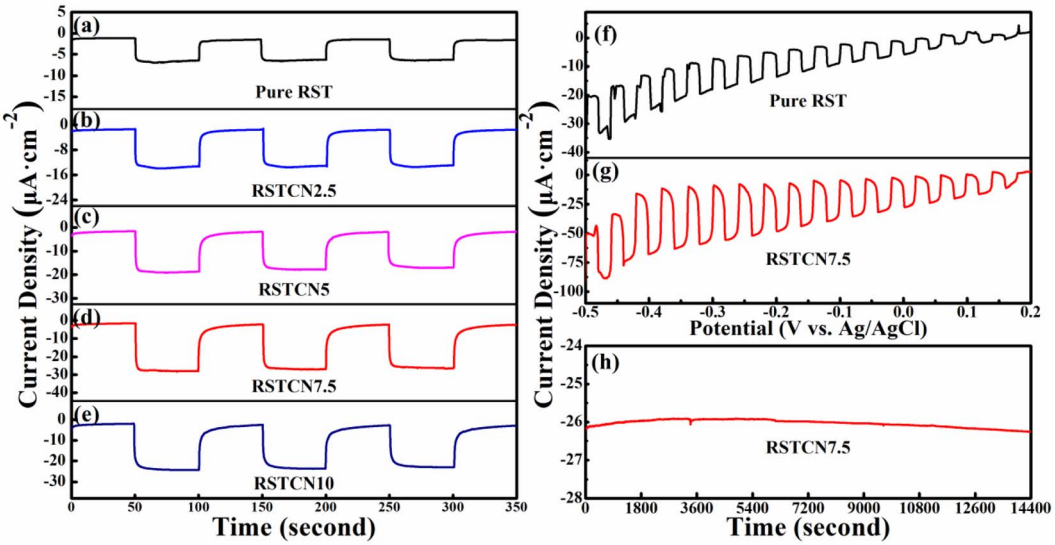

Fig. 3 PEC properties of different samples. Photocurrent *versus* time under chopped light (a) pure RST, (b) RSTCN2.5, (c) RSTCN5, (d) RSTCN7.5 and (e) RSTCN10. LSV curves under chopped light (f) pure RST and (g) RSTCN7.5 sample. (h) Longtime photocurrent *versus* time under light for 4 hours of RSTCN7.5 sample.

epitaxy (MBE) method.[11,35,36] To further observe the performance of the samples, the linear sweep voltammetry (LSV) curves of pure RST and RSTCN7.5 heterojunction samples were obtained under chopped light irradiation (Fig. 3f and g). The photocurrent density values have a steady increase with the increasing applied potential, and the good photocurrent responses are observed for each switch on and switch off in both RST and RSTCN7.5 heterojunction samples. Compared to pure RST sample, RSTCN7.5 heterojunction sample exhibited stronger response, indicating that the superior utilization of the light energy conversion. In addition, Fig. 3h shows the photocurrent stability test of the RSTCN7.5 sample in 0.5 M Na_2SO_4 solution under illumination for 4 hours, indicating the high stability of the PEC system.

3.4 Optical characterization

Generally, the improved PEC properties in semiconductor heterostructures can be attributed primarily to two factors. One factor is the enhanced light absorption capacity, whereas the other is the higher separation efficiency and transport properties of carrier.[37,38] Fig. 4a and S4a† demonstrates the absorption spectra of different samples. The absorption edge of pure $SrTiO_3$ was observed to be approximately 380 nm, located within the ultraviolet (UV) region. By doping of Rh element, the light absorption will be extended to the visible region. However, after incorporating g-C_3N_4, the optical absorption performance of the composite samples decreases, and the light absorption capacity of the composites diminishes with increasing g-C_3N_4 content. To gain more insights from the UV-vis absorption spectra, we can estimate the band gap energies of various samples by extrapolating the linear region of the $(\alpha h\nu)^2$ *versus* $(h\nu)$ plot to zero. Fig. S4b† displays that the band gap value of 3.26 eV in pure $SrTiO_3$ (Fig. S4b†), while the values of 1.65 and 2.65 eV can be obtained in RST sample (Fig. 4b). On referring to results and previous literature, the calculated values of 2.65 eV can be attributed to the electronic transitions from Rh^{3+} (electron donor levels) to conduction band of $SrTiO_3$, while that 1.65 eV can be attributed to the electronic transitions from valence band of $SrTiO_3$ to Rh^{4+} (electron acceptor levels).[13,14,16] For pure g-C_3N_4, the band gap value of g-C_3N_4 can be estimated to be 2.76 eV (Fig. 4c), that means the ability of light absorption in composite sample cannot be enhanced by decorating with g-C_3N_4 in composite sample, which is consistent with the absorption spectra. That is to say, it can be ruled out that the enhanced light absorption ability leads to the improvement of PEC performance in RSTCN heterojunctions.

3.5 PL analysis

To conduct a comprehensive assessment of the charge carrier separation and recombination process in different samples, the photoluminescence (PL) spectra were conducted. In general, PL emission primarily arises from the recombination of photogenerated electrons and holes in semiconductors, and a lower PL intensity indicates a reduced recombination rate of electron–hole pairs.[39] As shown in Fig. 4c, an emission peak at 450 nm, attributed to radiative carrier recombinations, can be observed in the pure RST sample. Compared to the RST sample, all RSTCN composites showed reduced PL intensity, indicating decreased carrier recombination rates. As the g-C_3N_4 content in the composites increases, the PL intensity initially decreases and then increases, with the RSTCN7.5 heterojunction sample showing the lowest PL peak intensity. The RSTCN10 sample exhibits a higher PL peak intensity compared to the RSTCN7.5 sample, indicating higher recombination rates, which lead to decreased PEC properties in the RSTCN10 sample. To further investigate the carrier separation and recombination processes

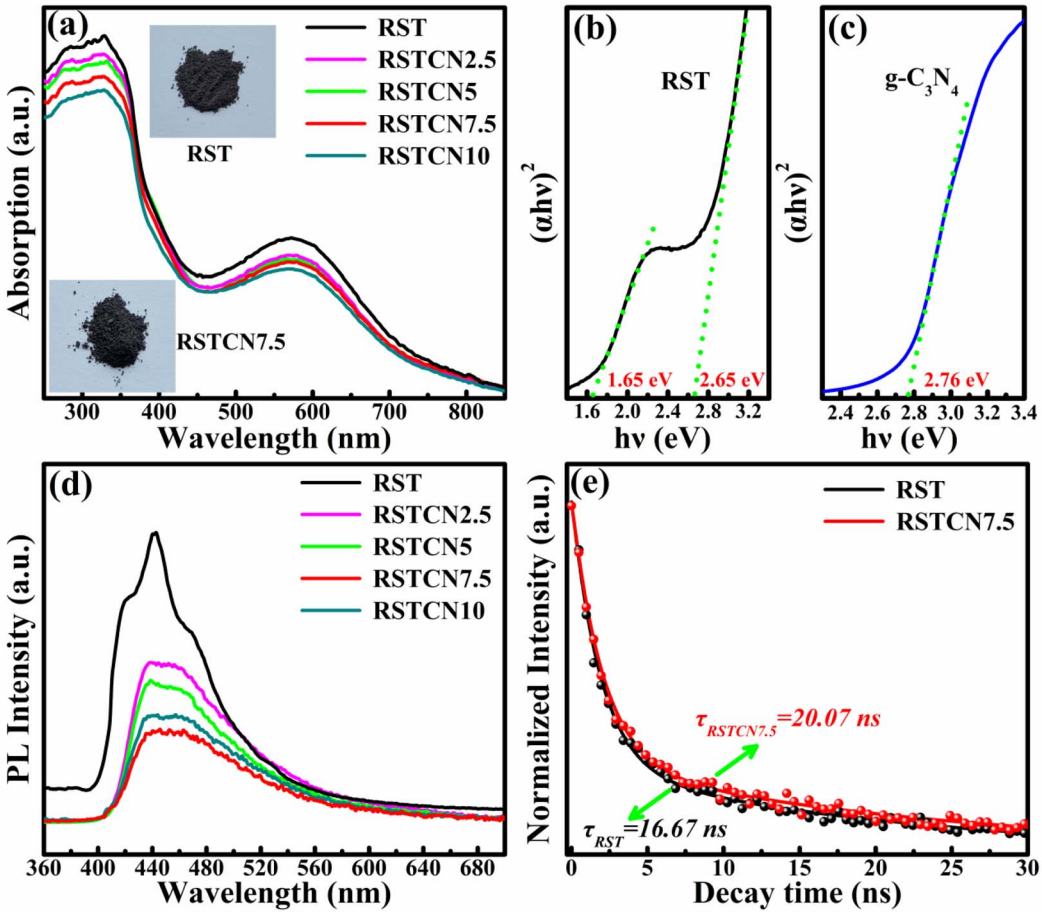

Fig. 4 Optical properties and carrier kinetics of different samples. (a) Absorption spectra of different samples. E_g values for (b) pure RST, (c) g-C_3N_4. (d) PL spectra of different samples, (e) PL-decay of RST and RSTCN7.5.

in the samples, PL decay curves for RST and RSTCN7.5 were recorded at a detection wavelength of 450 nm. The curves were fitted using the double exponential function $I(t) = A_1 \quad e(-t/\tau_1) + A_2 \quad e(-t/\tau_2) + I(0)$. The carrier lifetime can be determined by the $\tau = (A_1{\tau_1}^2 + A_2{\tau_2}^2)/(A_1\tau_1 + A_2\tau_2)$.[40] As shown in Fig. 5d and Table S1,† the carrier lifetimes for RST and RSTCN7.5 are 16.67 ns and 20.07 ns, respectively. Additionally, the PL peak intensity of pure g-C_3N_4 is higher than that of RST, while its carrier lifetime is shorter (Fig. S5 and Table S1†). Clearly, the RSTCN7.5 heterojunction sample exhibits the longest carrier lifetime, indicating superior separation efficiency and transmission performance of carriers within the composite material.

3.6 EIS analysis

To evaluate the kinetics of charge transfer process, electrochemical impedance spectroscopy (EIS) was conducted on various samples without light irradiation. Generally, the arc radius obtained from EIS serves as an indicator of the charge transfer resistance occurring at the interface between the semiconductor materials and the electrolyte.[41,42] As depicted in Fig. 5a, all samples exhibit only one arc, suggesting a significant resistance between the semiconductor photoelectrodes and electrolyte. In addition, the equivalent circuit (EC, inset of Fig. 5a) model was employed to fit the EIS data to enhance the analysis of EIS results. The fitting results are summarized in Table S2,† indicating that the charge transfer resistance (R_{ct}) at the semiconductor/electrolyte interface for the RSTCN7.5 heterojunction sample (3699 Ω) is significantly lower than that of the pure RST (6769 Ω). The reduced R_{ct} suggests a more efficient transfer of carriers across the interface to the electrolyte, thereby suppressing carrier recombination, which is consistent with the PL analysis. Moreover, the lower slope of Mott–Schottky (MS) curves in RSTCN7.5 sample also indicates that the higher charge carrier densities in heterojunction sample. Based on the results, the extended light absorption capacity leading to enhanced PEC properties of RSTCN heterojunction can be excluded. Instead, the enhanced PEC performance observed in RSTCN heterojunction can be attributed to the reduced recombination rates, improved carrier higher separation efficiency, and enhanced carrier transport properties.

3.7 Mott–Schottky and band edge positions

As shown in Fig. 5, the Mott–Schottky (MS) curves were employed to assess the semiconductor characteristics of different samples. The negative slope of linear segment for RST sample is investigated, which indicates its p-type semiconductor characteristics (Fig. 5b). The positive slope of linear segment for g-C_3N_4 material indicates its n-type characteristics

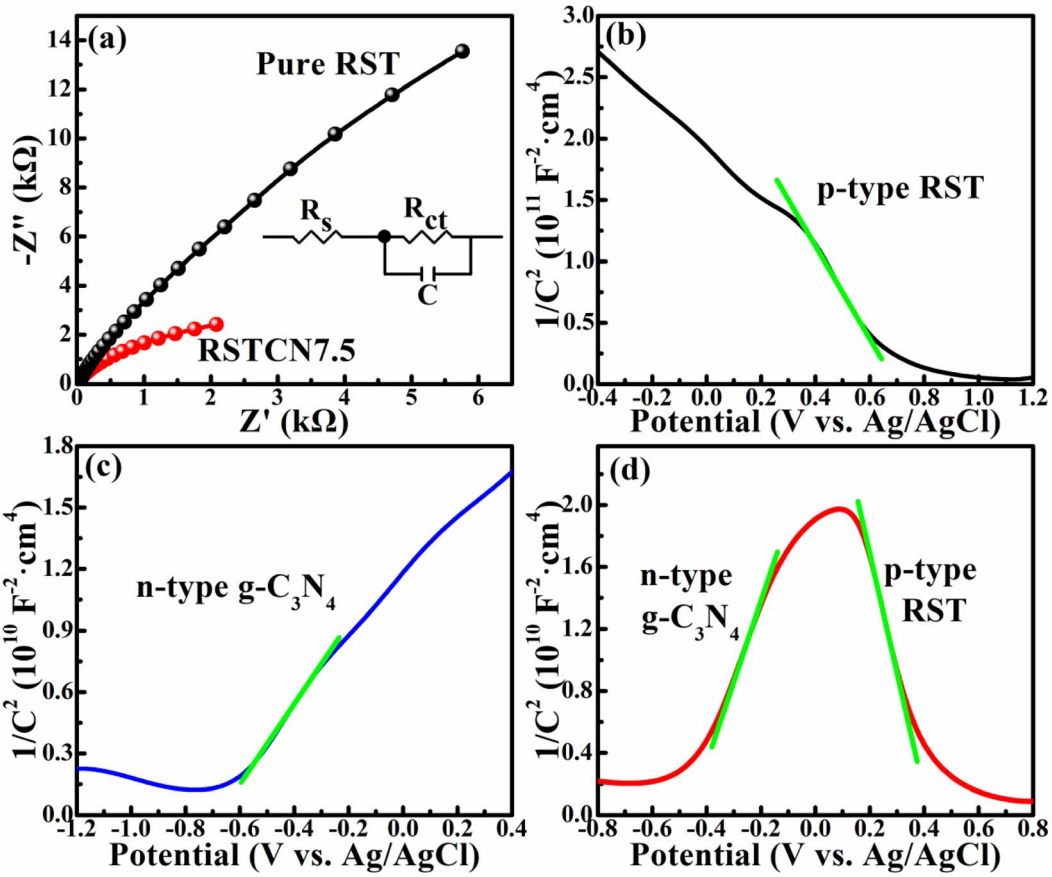

Fig. 5 (a) EIS of RST and RSTCN7.5 samples. Mott–Schottky curves of different samples. (b) RST, (c) g-C_3N_4, and (d) RSTCN7.5 heterojunction.

(Fig. 5c). However, the obtained MS curve exhibited a inverted "V" shape with two linear segments, indicating the existence of p–n junction in composite sample.[43,44] The linear segment with a negative and positive slope can be attributed to p-type RST and n-type g-C_3N_4 materials (Fig. 5d), respectively. In this study, the band edge positions at the point of zero charge can be determined by the following equations:[45,46]

$$E_{VB} = \chi - 4.5\ \text{eV} + 0.5 \times E_g \quad (1)$$

$$E_{CB} = E_{VB} - E_g \quad (2)$$

where the E_{CB}, E_{VB}, χ and E_g represent conduction band, valence band, electronegativity value, and the gap energies of semiconductors, respectively. The electronegativity value of $SrTiO_3$ is

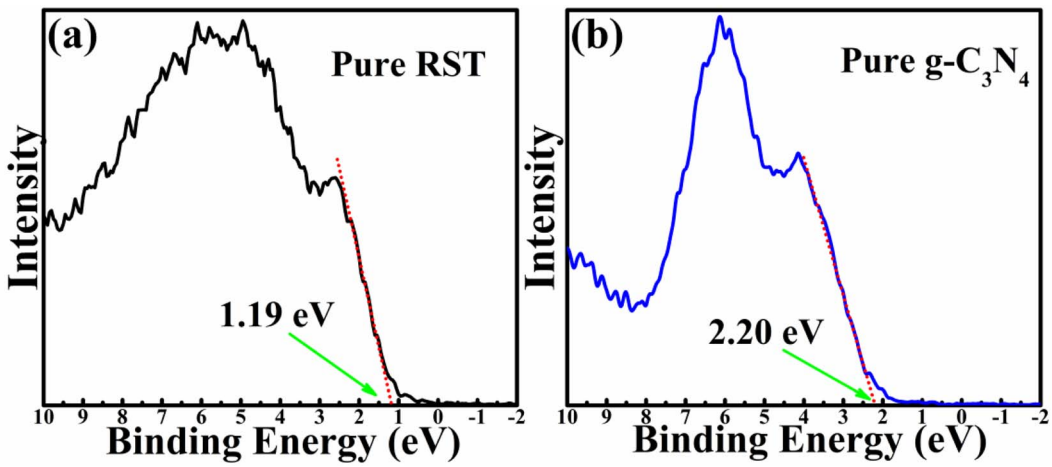

Fig. 6 XPS valence band spectra of different samples. (a) RST and (b) g-C_3N_4.

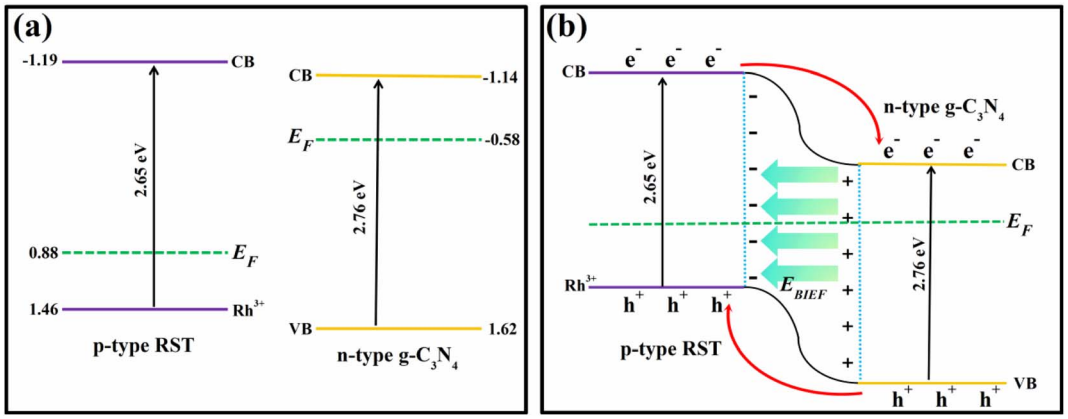

Fig. 7 Energy diagram for enhanced PEC performance. (a) Band edges position between RST and g-C_3N_4 before contact, (b) band alignment between RST and g-C_3N_4 after contact (E_{BIEF}: built-in electric field).

4.94 eV, while that of g-C_3N_4 is 4.74 eV, respectively.[45,46] According to empirical equations, the band positions of E_{CB} and E_{VB} in $SrTiO_3$ are −1.19 eV and 2.07 eV, respectively, while that in g-C_3N_4 are −1.14 eV and 1.62 eV, respectively. After doping Rh element, the band positions of Rh^{4+} and Rh^{3+} in RST are 1.46 eV and 0.42 eV, respectively. The relative difference between Fermi level (E_F) and E_{VB} ($E_F - E_{VB}$) of the semiconductors can be determined by extrapolating the linear region of XPS valence band spectra to zero. As shown in Fig. 6, the $E_F - E_{VB}$ value of RST is 1.19 eV, while the corresponding value of g-C_3N_4 is 2.20 eV.[24,30] In addition, the $E_F - E_{VB}$ value of RST is less than half of the bandgap due to its p-type semiconductor characteristic, whereas that of g-C_3N_4 exceeds half of the bandgap due to its n-type characteristic.

Based on the above analysis, the positions of pure RST, including Rh^{4+} and Rh^{3+} levels, are shown in Fig. S7.† The Rh^{4+} electron acceptor levels have insufficient potential for H_2 evolution, indicating that they do not significantly contribute to this process, consistent with previous studies.[10] Conversely, Rh^{3+} levels can serve as electron donors, transferring electrons to the E_{CB} of RST for H_2 evolution. Thus, the band position diagram of pure RST (before contact with g-C_3N_4) can be simplified, as depicted in Fig. 7a. The positions for g-C_3N_4 (before contact with RST) are also illustrated in Fig. 7a. After contact, electrons will flow from g-C_3N_4 to RST until the E_F levels reach equilibrium. After the equilibrium, the p-type RST and n-type g-C_3N_4 regions will have negative and positive charges, respectively, resulting in the formation of a built-in electric field (E_{BIEF}), oriented from g-C_3N_4 to RST with the well-matched energy band alignment.[47] Fig. 7b shows the energy band diagrams of the p–n junction between RST and g-C_3N_4. The E_{CB} of RST is more positive than that of the g-C_3N_4, whereas the E_{VB} of g-C_3N_4 is more negative than the Rh^{3+} of RST. Under light irradiation, the photogenerated electrons will migrate from the E_{CB} of RST to the E_{CB} of g-C_3N_4, whereas the photogenerated holes will migrate in the opposite direction, from the E_{VB} of g-C_3N_4 to the Rh^{3+} of RST. Such charge transfer process induced by p–n junction can greatly reduce the recombination rates and improve the transfer properties of carriers, leading to the enhanced PEC performance in RSTCN heterojunction sample.

4. Conclusions

In conclusion, a hybrid RSTCN p–n heterojunction was prepared by a simple method. The prepared RST photoelectrode demonstrates excellent visible light absorption capabilities and exhibits p-type semiconductor properties, yielding a photocurrent value of −6.2 μA cm^{-2} and demonstrating photocathodic behavior within the PEC system. After decorating with n-type g-C_3N_4 materials, all composite photoelectrodes demonstrated significantly enhanced PEC performance, characterized by increased photocurrent values. The optimized RSTCN7.5 heterojunction sample demonstrates a maximum photocurrent density of approximately −26.5 μA cm^{-2}, which is 4.3 times higher than that of the pure RST photoelectrode sample. The PL and EIS analyses revealed the presence of reduced recombination rates and enhanced carrier transfer properties in the heterojunction sample, which can be attributed to the efficient charge separation and transfer process caused by the formation of a p–n junction between RST and g-C_3N_4. The formed p–n junction, featuring a built-in electric field and well-matched energy band alignment, significantly suppresses carrier recombination rates and facilitate efficient separation and transfer of carriers, thereby leading to the enhanced PEC performance in heterojunction sample. This study provides a promising approach for the practical application development of high-performance PEC systems.

Data availability

All relevant data are available in the manuscript and the ESI.†

Conflicts of interest

There are no conflicts to declare in this paper.

Acknowledgements

This work was supported by the Natural Science Foundation of Jiangsu Higher Education Institutions of China (Grant No. 24KJA140002), the Natural Science Foundation of Jiangsu

Province (Grant No. BK20201476 & BK20201067), and the Guangdong Basic and Applied Basic Research Foundation (2023A1515011499).

References

1 A. Fujishima and K. Honda, *Nature*, 1972, **238**, 37–38.
2 H. Tong, S. X. Ouyang, Y. Bi, N. Umezawa, M. Oshikiri and J. H. Ye, *Adv. Mater.*, 2012, **24**, 229–251.
3 J. Q. Lv, J. F. Xie, A. G. A. Mohamed, X. Zhang and Y. B. Wang, *Chem. Soc. Rev.*, 2022, **51**, 1511–1528.
4 Y. X. Tan, X. Zhang, J. Lin and Y. B. Wang, *Energy Environ. Sci.*, 2023, **16**, 2432–2447.
5 Z. R. Wang and H. Einaga, *ChemCatChem*, 2023, **15**, e202300723.
6 M. A. Gaikwad, U. P. Suryawanshi, U. V. Ghorpade, J. S. Jang, M. P. Suryawanshi and J. H. Kim, *Small*, 2022, **18**, 2105084.
7 F. Li, J. Jian, Y. X. Xu, S. Y. Wang, H. Y. Wang and H. Q. Wang, *Eng. Rep.*, 2021, **3**, e12387.
8 B. Zutter, Z. J. Chen, L. Barrera, W. Gaieck, A. S. Lapp, K. Watanabe, A. Kudo, D. V. Esposito, R. B. Chandran, S. Ardo and A. A. Talin, *ACS Nano*, 2023, **17**, 9405–9414.
9 C. Zhen, X. T. Chen, R. T. Chen, F. T. Fan, X. X. Xu, Y. Y. Kang, J. D. Guo, L. Z. Wang, G. Q. Lu, K. Domen, H. M. Cheng and G. Liu, *Nat. Commun.*, 2024, **15**, 1672.
10 K. Iwashina and A. Kudo, *J. Am. Chem. Soc.*, 2011, **133**, 13272–13275.
11 S. Kawasaki, K. Nakatsuji, J. Yoshinobu, F. Komori, R. Takahashi, M. Lippmaa, K. Mase and A. Kudo, *Appl. Phys. Lett.*, 2012, **101**, 033910.
12 M. Antuch, P. Millet, A. Iwase and A. Kudo, *Electrochim. Acta*, 2019, **297**, 696–704.
13 R. Konta, T. Ishii, H. Kato and A. Kudo, *J. Phys. Chem. B*, 2004, **108**, 8992–8995.
14 S. Kawasaki, K. Akagi, K. Nakatsuji, S. Yamamoto, I. Matsuda, Y. Harada, J. Yoshinobu, F. Komori, R. Takahashi, M. Lippmaa, C. Sakai, H. Niwa, M. Oshima, K. Iwashina and A. Kudo, *J. Phys. Chem. C*, 2012, **116**, 24445–24448.
15 D. H. K. Murthy, H. Matsuzaki, Q. Wang, Y. Suzuki, K. Seki, T. Hisatomi, T. Yamada, A. Kudo, K. Domen and A. Furube, *Sustainable Energy Fuels*, 2019, **3**, 208–218.
16 M. Guo and G. J. Ma, *J. Catal.*, 2020, **391**, 241–246.
17 S. Okunaka, H. Tokudome and R. Abe, *Chem. Lett.*, 2016, **45**, 57–59.
18 R. P. Sugavaneshwar, K. Chen, G. Lakshminarayana, S. Ishii, T. D. Dao, N. Umezawa and T. Nagao, *APL Mater.*, 2015, **3**, 116103.
19 S. Zhang, E. H. Jiang, J. Wu, Z. H. Liu, Y. Yan, P. W. Huo and Y. S. Yan, *Catalysts*, 2023, **13**, 851.
20 D. Yazaki, T. Kawawaki, T. Tanaka, D. Hirayama, Y. Shingyouchia and Y. Negishi, *Energy Adv.*, 2023, **2**, 1148–1154.
21 B. Y. Zhang, K. W. Liu, Y. Xiang, J. M. Wang, W. R. Lin, M. Guo and G. J. Ma, *ACS Catal.*, 2022, **12**, 2415–2425.
22 W. J. Ong, L. L. Tan, Y. H. Ng, S. T. Yong and S. P. Chai, *Chem. Rev.*, 2016, **116**, 7159–7329.
23 A. Akhundi, A. Z. Moshfegh, A. H. Yangjeh and M. Sillanpää, *ACS ES&T Eng.*, 2022, **4**, 564–585.
24 L. X. Wang, Y. L. Dong, J. Y. Zhang, F. F. Tao and J. J. Xu, *J. Solid State Chem.*, 2022, **308**, 122878.
25 W. He, L. Liu, T. T. Ma, H. M. Han, J. J. Zhu, Y. P. Liu, Z. Fang, Z. Yang and K. Guo, *Appl. Catal., B*, 2022, **306**, 121107.
26 E. M. Hu, Q. Liu, Z. S. Qian, Q. Zhong, J. H. He, S. C. Xu, T. M. Lu, J. Li, T. Chen and W. K. Zhu, *Small*, 2024, **43**, 2403105.
27 Q. C. Feng, Z. Liu, R. D. Su, Y. Chen, Y. Wang, D. F. Ma and Q. Li, *Appl. Catal., B*, 2025, **362**, 124714.
28 B. Wang, P. Li, H. J. Hao, H. J. He, H. R. Cai, F. F. Shang, B. An, X. Q. Li and S. C. Yan, *Nanomaterials*, 2022, **12**, 4428.
29 A. Kumar, V. N. Rao, A. Kumar, A. Mushtaq, L. Sharma, A. Halder, S. K. Pal, M. V. Shankar and V. Krishnan, *ACS Appl. Energy Mater.*, 2020, **3**, 12134–12147.
30 M. Antuch, P. Millet, A. Iwase, A. Kudo, S. A. Grigorievd and Y. Z. Voloshin, *Electrochim. Acta*, 2017, **258**, 255–265.
31 L. L. Wang, G. G. Tang, S. Liu, H. L. Dong, Q. Q. Liu, J. F. Sun and H. Tang, *Chem. Eng. J.*, 2022, **428**, 131338.
32 J. Chen, M. G. Wang, J. Han and R. Guo, *J. Colloid Interface Sci.*, 2020, **562**, 313–321.
33 M. Khandelwal, C. V. Tran and J. B. In, *Appl. Surf. Sci.*, 2022, **576**, 151714.
34 M. Khandelwal, C. V. Tran, J. Lee and J. B. In, *Chem. Eng. J.*, 2022, **428**, 131119.
35 X. X. Zhao, Y. H. Sang, H. Liu and X. W. Yu, *Adv. Sustainable Syst.*, 2024, 2400756.
36 H. S. Lu, S. X. Song, Q. S. Jia, G. B. Liu and L. H. Jiang, *Acta Phys.-Chim. Sin.*, 2024, **40**, 2304035.
37 J. X. Low, J. G. Yu, M. Jaroniec, S. Wageh and A. A. Al-Ghamdi, Heterojunction Photocatalysts, *Adv. Mater.*, 2017, **29**, 1601694.
38 S. X. Zhong, Y. M. Xi, Q. Chen, J. R. Chen and S. Bai, *Nanoscale*, 2020, **12**, 5764–5791.
39 D. W. Cao, M. Li, J. F. Zhu, Y. F. He, T. Chen, Y. Liu, M. M. Chen and Y. Yang, *J. Semicond.*, 2021, **42**, 112701.
40 S. Wang, F. G. Zheng, Y. Y. Weng, G. L. Yuan, L. Fang and L. You, *Adv. Mater. Interfaces*, 2020, **10**, 2000185.
41 A. R. C. Bredar, A. L. Chown, A. R. Burton and B. H. Farnum, *ACS Appl. Energy Mater.*, 2020, **3**, 66–98.
42 A. Ch. Lazanas and M. I. Prodromidis, *ACS Meas. Sci. Au*, 2023, **3**, 162–193.
43 X. L. Liao, T. T. Li, H. T. Ren, Z. Y. Mao, X. F. Zhang, J. H. Lin and C. W. Lou, *Ceram. Int.*, 2021, **47**, 10786–10795.
44 Y. Z. Liu, S. S. Ding, J. Xu, H. Y. Zhang, S. G. Yang, X. G. Duan, H. Q. Sun and S. B. Wang, *Chin. J. Catal.*, 2017, **38**, 1052–1062.
45 Y. Xu and M. A. A. Schoonen, *Am. Mineral.*, 2000, **85**, 543–556.
46 S. Vignesh and H. Kim, *J. Alloys Compd.*, 2023, **942**, 169077.
47 X. Zhao, M. J. Liu, Y. C. Wang, Y. Xiong, P. Y. Yang, J. Q. Qin, X. Xiong and Y. P. Lei, *ACS Nano*, 2022, **16**, 19959–19979.